Strong Gravitational Lensing and Shadow Signatures of Anisotropic Black Holes in Plasma*

Pakhlavon Yovkochev[1†] Atamurotov Farruh[2,3‡] Abdujabbarov Ahmadjon[1,4§] Yerzhanov Koblandy[5♮]
Bauyrzhan Gulnur[5♯] Chengxun Yuan (袁承勋)[4¶]

[1]Institute of Fundamental and Applied Research, National Research University TIIAME, Kori Niyoziy 39, Tashkent 100000, Uzbekistan
[2]Inha University in Tashkent, Ziyolilar 9, Tashkent 100170, Uzbekistan
[3]University of Tashkent for Applied Sciences, Str. Gavhar 1, Tashkent 100149, Uzbekistan
[4]School of Physics, Harbin Institute of Technology, Harbin 150001, People's Republic of China
[5]L.N. Gumilyov Eurasian National University, Astana 010008, Kazakhstan

Abstract: We study strong gravitational lensing and black hole shadow in a static, spherically symmetric spacetime sourced by anisotropic matter with exponentially decaying hair, in the presence of a non-magnetized plasma. The geometry is characterized by deformation parameters $\tilde{\upsilon}_2$ and $\tilde{\upsilon}_c$, which influence the photon sphere and shadow in opposing ways: $\tilde{\upsilon}_2$ shrinks both while $\tilde{\upsilon}_c$ enlarges them. Plasma effects systematically increase the shadow size and suppress the deflection angle. Using EHT observations of Sgr A*, we constrain the parameter space of the model. Our analysis demonstrates that anisotropic matter hair and plasma environments produce distinguishable signatures in strong-field gravitational optics, offering potential probes for testing deviations from the standard gravity.

Keywords: aaaa

DOI: 10.1088/1674-1137/ae7706 **CSTR:** 32044.14.ChinesePhysicsC.

I. INTRODUCTION

The study of black hole spacetimes has progressed significantly from the simplest vacuum solutions to more realistic configurations that account for surrounding matter fields. While the Schwarzschild metric remains the paradigmatic description of a static, spherically symmetric black hole in vacuum, astrophysical black holes are seldom isolated; they often reside in environments enriched with dark matter, dark energy, or other anisotropic matter distributions. This motivates the search for exact solutions of the Einstein equations that describe black holes coexisting with non-trivial matter fields. In a recent work, Kim et al. [1] presented a new static, spherically symmetric black hole solution that extends the Schwarzschild spacetime by incorporating an anisotropic matter field, where the function $\upsilon(r) = \upsilon_2 e^{-\upsilon_c r^2/2}$ (up to subleading terms) yields an energy density that decays exponentially with the radial distance. This behavior introduces a new form of black hole "hair" that is localized near the horizon and remains undetectable to asymptotic observers, thereby circumventing the standard no-hair arguments [2–4]. The matter supporting this geometry satisfies an equation of state with radial pressure equal to the negative of the energy density, reminiscent of electromagnetic fields but with an exponential fall-off that gives rise to novel thermodynamic properties. Such a solution provides an ideal testing ground for exploring observational signatures of anisotropic matter near black holes, since the modification of metric functions directly alters the location of the event horizon, which in turn affects the shape and size of the black hole shadow as well as the strong gravitational lensing observables, offering a richer phenomenology that can potentially be constrained by Event Horizon Telescope observations [5–7].

The pursuit of a complete theory of gravity necessitates rigorous experimental and observational tests across all regimes. Although general relativity (GR) has passed a multitude of tests in the weak-field regime, from solar system dynamics [8] to binary pulsar observations [9], its

Received 23 March 2026; Accepted 3 June 2026

* This research was funded by the National Natural Science Foundation of China (NSFC) under Grant No. U2541210. This research is funded by the Science Committee of the Ministry of Science and Higher Education of the Republic of Kazakhstan (Grant No. AP23489289)

† E-mail: yovqochevp@gmail.com
‡ E-mail: atamurotov@yahoo.com
§ E-mail: ahmadjon@astrin.uz
♮ E-mail: yerzhanovkk@gmail.com
♯ E-mail: bauyrzhan.g.b@gmail.com
¶ E-mail: yuancx@hit.edu.cn

validity in the strong-field regime remains an active area of investigation. This regime, characterized by intense gravitational fields and large spacetime curvature, is where deviations from GR are most likely to manifest. In this context, the motion of test particles and photons in curved spacetimes serves as a fundamental probe of gravitational theory. Unlike weak-field tests, which are often well-described by parameterized post-Newtonian (PPN) frameworks, strong-field environments require exact solutions of the Einstein equations and a careful analysis of geodesic motion. The trajectories of stars, accretion flows, and photons near compact objects encode the underlying spacetime geometry with exceptional precision, making them indispensable tools for discriminating between GR and alternative theories of gravity [10−12].

The motion of test particles and photons in curved spacetimes provides a powerful diagnostic for probing the underlying gravitational theory [13]. More recently, attention has turned to the observational signatures of modified gravity, particularly gravitational lensing and photon motion, which offer direct windows into the strong-field regime [14−19]. Among the most promising observational probes of strong-field gravity are the shadow of a black hole and the phenomenon of strong gravitational lensing. The black hole shadow, a dark region cast by the event horizon against the surrounding emission, is a direct imprint of the spacetime geometry near the photon sphere and provides a powerful tool to extract information about the properties of compact objects. In vacuum, the properties of black hole shadows have been extensively studied and are well understood, providing a fundamental baseline for interpreting observational signatures of compact objects [20−27]. The Event Horizon Telescope (EHT) has achieved the remarkable feat of resolving the shadows of M87* and Sagittarius A* [5−7], opening a new window for testing gravity under the most extreme conditions. These observables are highly sensitive to deviations from standard gravity and thus provide a powerful avenue to test gravitational theories [28−30]. However, in realistic astrophysical scenarios, compact objects are typically surrounded by plasma, which can significantly influence the propagation of light. In such a dispersive medium, both gravitational lensing and black hole shadow characteristics become frequency-dependent, leading to observable deviations from the vacuum case. A growing body of work has investigated the impact of plasma medium on the light deflection, lensing observables, and shadow formation, demonstrating that plasma effects can alter the size and brightness of the black hole's shadow [31−36]. Several studies have also explored gravitational lensing and black hole shadow formation in plasma environments and within modified or alternative theories of gravity, showing that both dispersive media and deviations from standard geometry can significantly affect observable features [37−48].

In this work, we plan to systematically investigate the strong gravitational lensing and shadow properties of the black hole with anisotropic matter described by the metric presented in [1], extending the analysis to include the effects of a surrounding non-magnetized plasma. By considering both homogeneous and inhomogeneous plasma distributions, we examine how the exponentially decaying hair encoded in the deformation parameters influences the photon sphere, the shadow size, and the strong-field deflection angle of light. We further employ observational constraints from the Event Horizon Telescope's Sgr A* shadow measurement to restrict the viable parameter space of the model, thereby assessing the potential detectability of such anisotropic matter configurations through future high-precision black hole imaging and lensing observations. In particular, the paper is organized as follows: we formulate the equations of motion of photons in Sect. II. The Sect. III is devoted to analysis of photon sphere. Black shadow and strong lensing around black holes dressed with anisotropic matter have been explored in Sects. IV and V, respectively. We conclude our results in Sect. VI. Throughout the paper, we use a system of geometric units in which $G=1=c$. The Greek (Latin) indices run from 0 (1) to 3.

II. EQUATIONS OF MOTION FOR LIGHT RAYS IN A NON-MAGNETIZED PLASMA

We consider the action [1]

$$I=\int d^4x\sqrt{-g}\left(\frac{R}{2\kappa}+\mathcal{L}_{\rm am}\right)+I_{\rm b}, \tag{1}$$

where $\kappa=8\pi G$, $\mathcal{L}_{\rm am}$ is the Lagrangian density of an effective anisotropic matter field, and $I_{\rm b}$ denotes the boundary term required for a well-defined variational principle.

Varying the action with respect to the metric yields the Einstein field equations

$$G_{\mu\nu}=R_{\mu\nu}-\frac{1}{2}Rg_{\mu\nu}=\kappa T_{\mu\nu}, \tag{2}$$

where the stress-energy tensor $T_{\mu\nu}$ is derived from the matter Lagrangian $\mathcal{L}_{\rm am}$.

For the anisotropic matter distribution under consideration, the stress-energy tensor takes the diagonal form

$$T^{\mu}{}_{\nu}={\rm diag}(-\varepsilon,p_r,p_t,p_t), \tag{3}$$

with ε the energy density, p_r the radial pressure, and p_t the tangential pressure. The anisotropy of the fluid is characterized by the inequality $p_r\neq p_t$, which distinguishes it from a perfect fluid configuration where the pressures are isotropic.

Following Ref. [1], the energy density and pressures for this anisotropic matter field are given by

$$\varepsilon = \frac{v_2 e^{-v_c r^2/2}}{\kappa r^4}, \tag{4}$$

$$p_r = -\varepsilon, \tag{5}$$

$$p_t = \left(1 + \frac{v_c r^2}{2}\right)\varepsilon, \tag{6}$$

where v_2 and v_c are positive constants that characterize the strength and the spatial decay scale of the matter distribution, respectively. The condition $p_r = -\varepsilon$ represents a negative radial pressure (tension), a feature typical of anisotropic matter distributions and commonly encountered in the stress-energy tensor of electromagnetic fields, while the tangential pressure acquires an additional positive contribution proportional to $v_c r^2$.

Fig. 1 illustrates the radial behavior of the energy density for different values of the parameters v_2 and v_c. The energy density remains positive and monotonically decreasing for all cases, exhibiting a rapid decay at large radii. In Fig. 1(a), for fixed $v_c = 0.1$, increasing v_2 enhances the magnitude of the energy density without altering its profile, indicating that v_2 controls the overall strength of the matter distribution. In contrast, Fig. 1(b) shows that increasing v_c leads to a faster decay of $\varepsilon(r)$, demonstrating that v_c determines the spatial localization of the matter field.

As shown in Fig. 1, the energy density diverges as $r \to 0$, indicating a central curvature singularity. However, the event horizon at $r = r_h$ encloses this singular region, so the physically relevant exterior spacetime remains regular for photon propagation. Since the shadow and lensing observables are determined by null geodesics outside the horizon, the central singularity does not affect the analysis.

The radial pressure is negative, $p_r = -\varepsilon$, while the tangential pressure $p_t = (1 + v_c r^2/2)\varepsilon$ remains positive and increases with radius, leading to a positive anisotropy factor throughout the spacetime.

We can now examine the energy conditions satisfied by the anisotropic matter source. Since $\varepsilon(r) > 0$ for all $r > 0$, the energy density remains positive everywhere outside the central singularity. The null and weak energy conditions are satisfied, with $\varepsilon + p_r = 0$ and $\varepsilon + p_t = (2 + v_c r^2/2)\varepsilon > 0$, indicating that the matter source is physically admissible in the standard sense. The strong energy condition is also satisfied, since $\varepsilon + p_r + 2p_t = (2 + v_c r^2)\varepsilon > 0$. However, the dominant energy condition is violated in the tangential direction because $p_t > \varepsilon$. This reflects the strongly anisotropic nature of the matter distribution and distinguishes it from ordinary perfect-fluid matter.

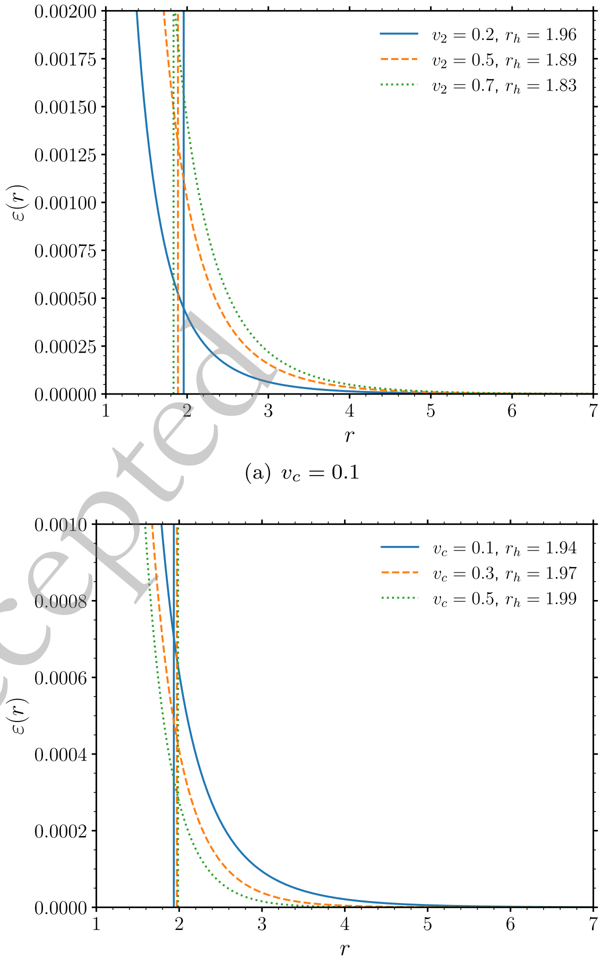

(a) $v_c = 0.1$

(b) $v_2 = 0.3$

Fig. 1. (color online) Radial behavior of the energy density for different values of the parameters v_2 and v_c. The vertical lines indicate the location of the event horizons $r = r_h$ for the corresponding parameter set.

We consider a static, spherically symmetric spacetime described by the line element

$$ds^2 = -f(r)dt^2 + \frac{1}{f(r)}dr^2 + r^2\left(d\theta^2 + \sin^2\theta\, d\phi^2\right). \tag{7}$$

Solving the Einstein equations with the stress-energy tensor given above, the metric function takes the form [1]

$$f(r) = 1 - \frac{2M}{r} + G(r), \tag{8}$$

where the deformation function $G(r)$ encodes the contribution of the anisotropic matter:

$$G(r) = \frac{v_2}{r^2}\left(e^{-\frac{v_c r^2}{2}} + r\sqrt{\frac{\pi v_c}{2}}\left[\mathrm{erf}\left(r\sqrt{\frac{v_c}{2}}\right) - 1\right]\right), \tag{9}$$

where erf(x) is the standard error function. In the limit $v_2 \to 0$, the Schwarzschild solution is recovered. For $v_c \to 0$ with $v_2 \neq 0$, the metric approaches a Reissner–Nordström–type configuration, where v_2 effectively plays the role of a charge parameter. The presence of the error function ensures that the matter distribution decays exponentially at large radii, localizing its effects near the black hole horizon.

For numerical analysis, we introduce dimensionless variables by rescaling all quantities with respect to the black hole mass M:

$$\tilde{v}_2 = \frac{v_2}{M^2}, \qquad \tilde{v}_c = v_c M^2. \tag{10}$$

Figure 2(a) shows the behavior of $f(r)$ for representative values of $\tilde{v}_2$ at fixed $\tilde{v}_c = 0.1$. For sufficiently small $\tilde{v}_2$, the metric function admits two positive roots, corresponding to an inner and an outer event horizon, analogous to the Reissner–Nordström geometry. As $\tilde{v}_2$ increases, these horizons approach each other and merge at a critical value $\tilde{v}_2 = \tilde{v}_{2,\mathrm{ext}}$, corresponding to an extremal black hole configuration. Beyond this critical value, the metric function no longer crosses zero, and the central singularity becomes naked. The full horizon structure in parameter space $(\tilde{v}_2, \tilde{v}_c)$ is summarized in Fig. 2(b). The extremal curve separates the black hole region, where the singularity is hidden behind horizons, from the naked singularity region, where no event horizon exists. In the present work, our analysis of photon spheres, shadows, and strong lensing is restricted to the black hole sector of the parameter space $(\tilde{v}_2, \tilde{v}_c)$, ensuring that all observables are computed in the regular exterior region.

We now assume that the spacetime is filled with a cold, non-magnetized plasma whose electron plasma frequency depends only on the radial coordinate [49]:

$$\omega_p^2(r) = \frac{4\pi e^2}{m_e} N(r), \tag{11}$$

where e and m_e denote the charge and mass of the electrons, respectively, and $N(r)$ is the density of the number of electrons. The refractive index of the plasma is defined as

$$n^2 = 1 - \frac{\omega_p^2(r)}{\omega^2(r)}. \tag{12}$$

The photon frequency measured by a static observer is obtained from gravitational redshift:

$$\omega(r) = \frac{\omega_0}{\sqrt{f(r)}}, \tag{13}$$

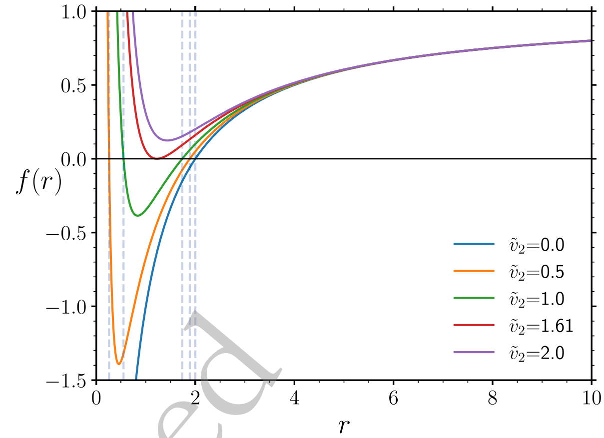

(a) Metric function $f(r)$ for the different values of $\tilde{v}_2$ at fixed $\tilde{v}_c = 0.1$. The zeros of $f(r)$ determine the horizon radii.

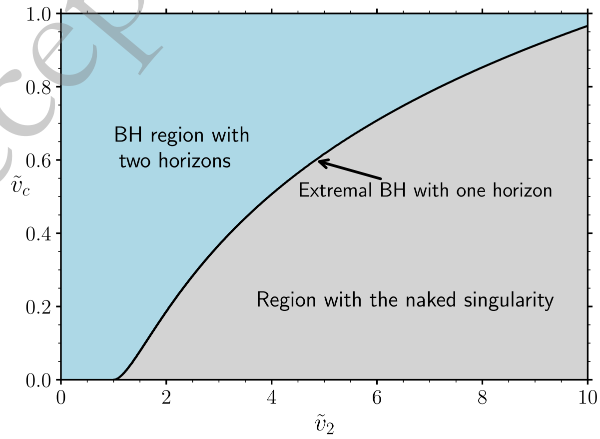

(b) Parameter-space structure in the $(\tilde{v}_2, \tilde{v}_c)$ plane showing black hole with two, one horizon and horizonless regions.

Fig. 2. (color online) Horizon analysis of the anisotropic black hole spacetime.

where $\omega_0 = -p_t$ is the conserved photon energy measured at spatial infinity. Photon propagation is possible only if $\omega^2(r) > \omega_p^2(r)$, ensuring a real refractive index.

Following Synge [50], the Hamiltonian describing photon motion in a plasma is

$$H(x^\alpha, p_\alpha) = \frac{1}{2}\tilde{g}^{\alpha\beta} p_\alpha p_\beta, \tag{14}$$

where x^α denote spacetime coordinates and p_α is the photon four-momentum. The effective metric is given by

$$\tilde{g}^{\alpha\beta} = g^{\alpha\beta} - (n^2 - 1)u^\alpha u^\beta, \tag{15}$$

with $u^\alpha = (1/\sqrt{f}, 0, 0, 0)$ being the four-velocity of the static plasma.

Restricting motion to the equatorial plane $(\theta = \pi/2)$, Hamilton's equations $\dot{x}^\alpha = \partial H/\partial p_\alpha$ yield [31]

$$\dot{t} = \frac{-p_t}{f(r)}, \tag{16}$$

$$\dot{r} = p_r f(r), \tag{17}$$

$$\dot{\phi} = \frac{p_\phi}{r^2}. \tag{18}$$

The trajectory equation then becomes

$$\frac{dr}{d\phi} = f(r)\frac{r^2 p_r}{p_\phi}. \tag{19}$$

Using the constraint $H = 0$, together with $p_t = -\omega_0$ and Eq. (12), we obtain [31]

$$\frac{dr}{d\phi} = \pm r\sqrt{f(r)}\sqrt{h^2(r)\frac{\omega_0^2}{p_\phi^2} - 1}, \tag{20}$$

where

$$h^2(r) = r^2\left[\frac{1}{f(r)} - \frac{\omega_p^2(r)}{\omega_0^2}\right]. \tag{21}$$

The function $h(r)$ generalizes the impact parameter in the presence of plasma.

III. PHOTON SPHERE

The radius of the unstable circular photon orbit, which defines the photon sphere $r_{\rm ph}$, is determined by the extremum condition of the generalized impact parameter function $h(r)$ [31],

$$\frac{d}{dr}\left(h^2(r)\right)\Big|_{r=r_{\rm ph}} = 0. \tag{22}$$

In general, due to the nontrivial structure of the metric function and the plasma contribution, Eq. (22) does not admit analytic solutions. Therefore, the photon sphere radius is determined numerically for representative plasma profiles.

A. Homogeneous plasma with $\omega_p^2(r) = \text{const.}$

We first consider a homogeneous plasma with constant plasma frequency, $\omega_p^2(r) = \text{const.}$. The corresponding radii of the photon sphere are shown in Fig. 3 for different values of the matter parameters $\tilde{\nu}_2$ and $\tilde{\nu}_c$, and for several ratios ω_p^2/ω_0^2.

In Fig. 3(a), where $\tilde{\nu}_c$ is fixed and $\tilde{\nu}_2$ is varied, the radius of the photon sphere decreases monotonically with increasing $\tilde{\nu}_2$. In the limit $\tilde{\nu}_2 \to 0$, the curves approach the

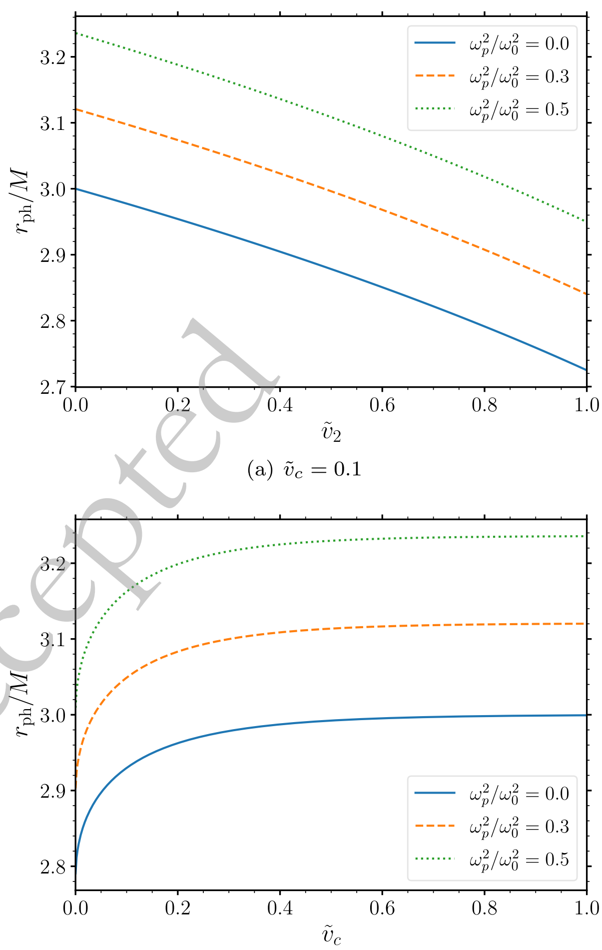

(b) $\tilde{\nu}_2 = 0.3$

Fig. 3. (color online) Photon sphere radius $r_{\rm ph}/M$ for a homogeneous plasma with constant plasma frequency.

Schwarzschild–plasma configuration, and in the vacuum limit $\omega_p(r) \equiv 0$ one recovers $r_{\rm ph} = 3M$. This behavior indicates that the deformation controlled by $\tilde{\nu}_2$ shifts the unstable circular photon orbit inward, effectively reducing the strength of the gravitational potential near the photon sphere.

For fixed $\tilde{\nu}_2$, increasing the ratio ω_p^2/ω_0^2 leads to a systematic outward shift of $r_{\rm ph}$. This reflects the refractive nature of the plasma: since the effective photon propagation speed is reduced, the unstable circular orbit occurs at larger radii.

Fig. 3(b) shows the dependence of $r_{\rm ph}$ on $\tilde{\nu}_c$ for fixed $\tilde{\nu}_2$. In contrast to $\tilde{\nu}_2$, the photon sphere radius increases monotonically with $\tilde{\nu}_c$ and approaches a saturation value for sufficiently large $\tilde{\nu}_c$. In the limit $\tilde{\nu}_c \to 0$, the geometry reduces to the Reissner–Nordström–type configuration governed by $\tilde{\nu}_2$, and the corresponding vacuum photon sphere is recovered [51]. The parameter $\tilde{\nu}_c$ therefore strengthens the effective gravitational field at small radii, pushing the unstable photon orbit outward.

The opposite effects of $\tilde{\nu}_2$ and $\tilde{\nu}_c$ can be understood directly from the anisotropic matter distribution in Eq. (6). The parameter $\tilde{v}_2$ controls the overall strength of the matter density and pressure components, acting as an amplitude factor. Therefore, increasing $\tilde{v}_2$ enhances the matter contribution to the spacetime geometry and produces a stronger local deformation near the photon orbit, shifting the unstable circular photon orbit inward and reducing $r_{\rm ph}$. By contrast, $\tilde{v}_c$ controls the exponential decay scale of the matter distribution. Larger values of $\tilde{v}_c$ cause the matter density to decay more rapidly with radius, making the matter configuration more compact and concentrated closer to the black hole. This redistribution modifies the geometry differently from a simple amplitude enhancement and shifts the effective potential barrier outward, resulting in a larger photon sphere radius. Thus, $\tilde{v}_2$ and $\tilde{v}_c$ play distinct physical roles: the former sets the strength of the matter source, while the latter determines its spatial localization.

Overall, in a homogeneous plasma environment, the refractive medium consistently enlarges the photon sphere relative to the corresponding vacuum configuration. While $\tilde{v}_2$ and $\tilde{v}_c$ influence $r_{\rm ph}$ in opposite qualitative directions, the plasma contribution always increases its radius.

B. Inhomogeneous plasma with $\omega_p^2(r) = z_0/r^q$ [52]

We now consider an inhomogeneous plasma described by the power-law profile $\omega_p^2(r) = z_0/r^q$ for two representative values of the power index, $q = 1$ and $q = 3$, as shown in Fig. 4.

For both values of q, the qualitative dependence of the photon sphere radius on the matter parameters remains the same as in the homogeneous plasma case: $r_{\rm ph}$ decreases monotonically with increasing $\tilde{v}_2$ and increases monotonically with increasing $\tilde{v}_c$. This demonstrates that the primary control over the photon sphere location arises from the spacetime deformation encoded in the metric function.

Quantitative differences, however, appear between the two plasma profiles. In the $q = 1$ case, increasing the plasma strength parameter z_0 produces a noticeable outward displacement of $r_{\rm ph}$, although the separation

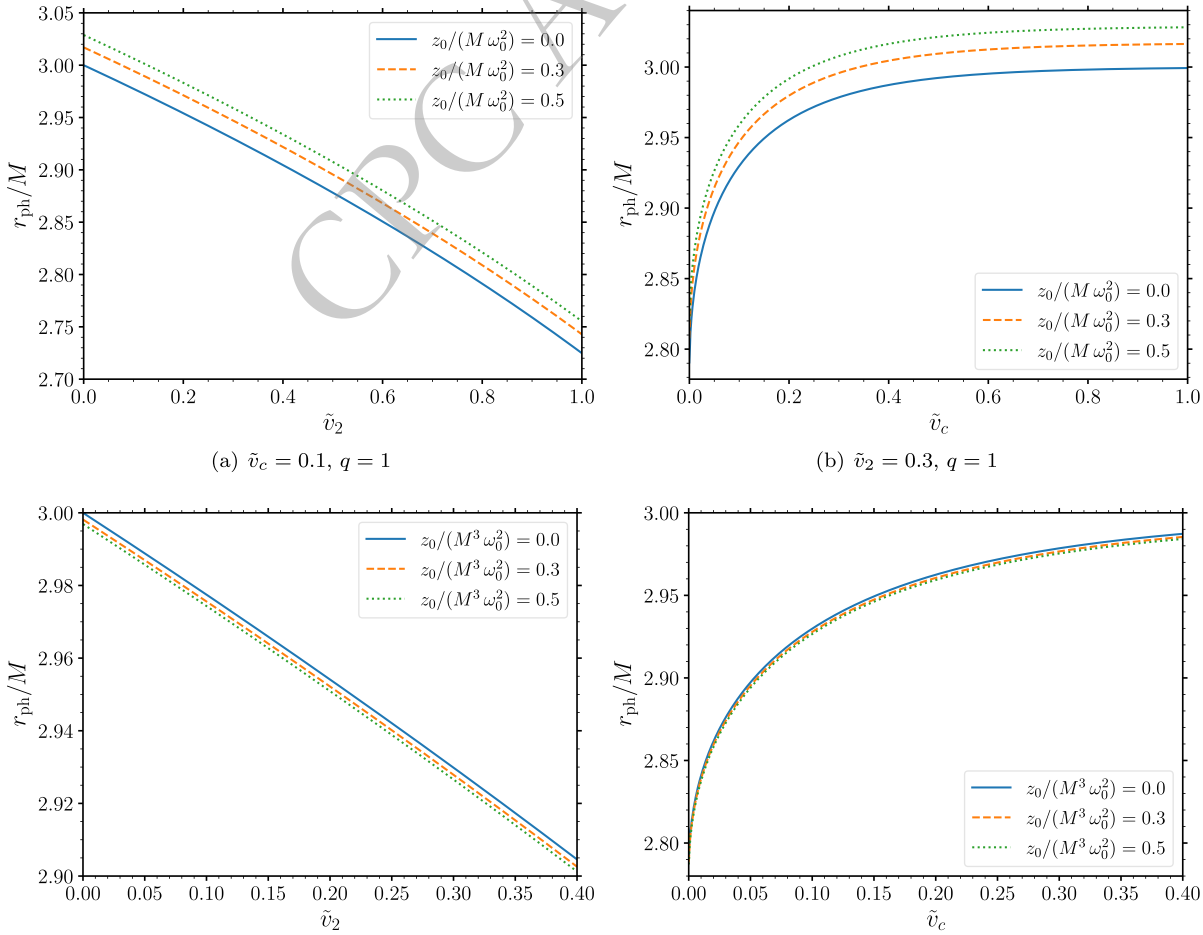

(a) $\tilde{v}_c = 0.1$, $q = 1$ (b) $\tilde{v}_2 = 0.3$, $q = 1$

(c) $\tilde{v}_c = 0.1$, $q = 3$ (d) $\tilde{v}_2 = 0.3$, $q = 3$

Fig. 4. (color online) Photon sphere radius $r_{\rm ph}/M$ for an inhomogeneous plasma with power-law plasma frequency for $q = 1$ (top row) and $q = 3$ (bottom row).

between curves corresponding to different z_0 values is smaller than in the homogeneous case. The slowly decaying plasma density therefore retains a measurable refractive influence near the photon orbit.

In contrast, for $q = 3$, the plasma effect becomes strongly suppressed. The curves corresponding to different values of z_0 are nearly indistinguishable, indicating that the photon sphere is almost entirely governed by the matter-deformed geometry. This behavior is expected since a steeper radial decay rapidly reduces the plasma density at radii relevant for the unstable circular orbit.

These results show that the refractive modification of the photon sphere depends sensitively on the radial falloff of the plasma frequency. Slowly decaying plasma distributions can produce observable corrections to $r_{\rm ph}$, whereas rapidly decreasing profiles yield negligible deviations. Consequently, unless the plasma density decreases sufficiently slowly with radius, the location of the photon sphere is predominantly determined by the spacetime deformation parameters $\tilde{v}_2$ and $\tilde{v}_c$.

IV. BLACK HOLE SHADOW IN A PLASMA-FILLED MATTER-DEFORMED SPACETIME

We now investigate the shadow cast by the black hole described by the metric (7) in the presence of a refractive plasma. The boundary of the shadow is determined by the unstable circular photon orbit at the photon sphere radius $r_{\rm ph}$ and depends on both the spacetime geometry and the plasma distribution.

For a static, spherically symmetric spacetime filled with a static plasma, the angular radius $\alpha_{\rm sh}$ of the shadow, as measured by an observer located at $r = r_{\rm o}$, is given by [20, 31]

$$\sin^2\alpha_{\rm sh} = \frac{h^2(r_{\rm ph})}{h^2(r_{\rm o})}, \tag{23}$$

where $h(r)$ is defined in Eq. (21).

For observationally relevant situations, we assume that the observer is located in a region where the plasma density is negligibly small [31]. Under this assumption, one has $h^2(r_o) \simeq r_o^2$, and the shadow radius on the observer's sky is

$$R_{\rm sh} = r_{\rm o}\sin\alpha_{\rm sh} = r_{\rm ph}\sqrt{\frac{1}{f(r_{\rm ph})} - \frac{\omega_p^2(r_{\rm ph})}{\omega_0^2}}. \tag{24}$$

This expression shows explicitly that the shadow size is controlled both by the location of the photon sphere and by the refractive properties of the plasma. In the vacuum limit $\omega_p(r) = 0$, Eq. (24) reduces to the standard geometric-optics result.

A. Homogeneous plasma

We first consider the homogeneous plasma approximation, where the plasma frequency is taken to be approximately constant in the vicinity of the black hole, $\omega_p^2(r) = \omega_c^2$. Following Ref. [31], we assume that the observer is located in a region where the plasma density is negligibly small, so that the standard far-observer approximation remains applicable.

The corresponding shadow radii are shown in Fig. 5 for different values of the matter parameters $\tilde{v}_2$ and $\tilde{v}_c$, and for several ratios ω_c^2/ω_0^2.

In Fig. 5(a), where $\tilde{v}_c$ is fixed, the shadow radius decreases monotonically with increasing $\tilde{v}_2$. This behavior mirrors the inward shift of the photon sphere discussed in Sec. 3. The parameter $\tilde{v}_2$ reduces the critical impact parameter and consequently shrinks the shadow.

For fixed $\tilde{v}_2$, increasing the plasma frequency leads to a systematic enlargement of the shadow. The refractive medium modifies the effective optical geometry, increasing the critical impact parameter and shifting the shadow

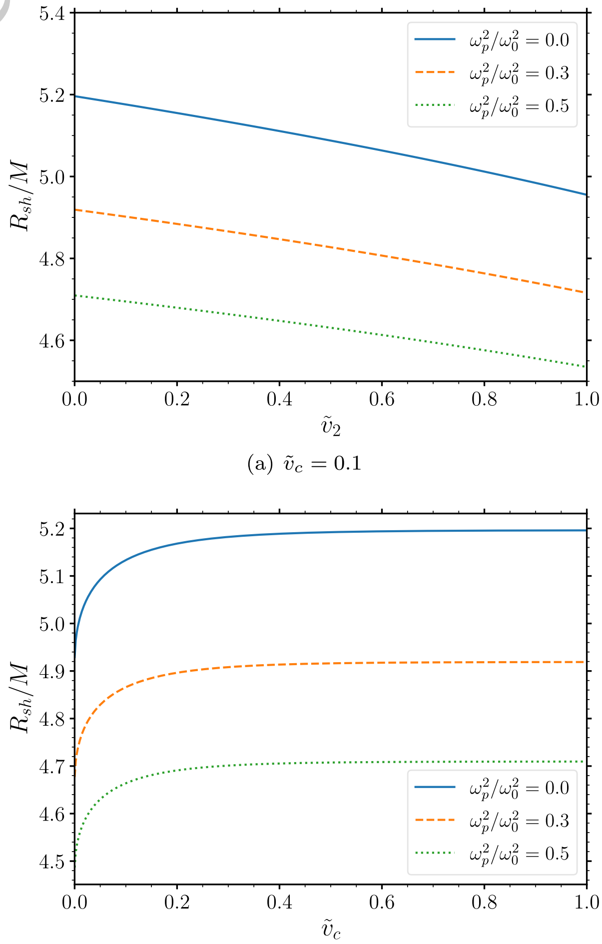

(b) $\tilde{v}_2 = 0.3$

Fig. 5. (color online) Shadow radius $R_{\rm sh}/M$ for the homogeneous plasma approximation with constant plasma frequency in the near-black-hole region.

boundary outward.

Figure 5(b) shows the dependence of $R_{\rm sh}$ on $\tilde{v}_c$ for fixed $\tilde{v}_2$. In contrast to $\tilde{v}_2$, the shadow radius increases monotonically with $\tilde{v}_c$ and approaches a saturation value at large $\tilde{v}_c$. This trend reflects the outward displacement of the photon sphere induced by $\tilde{v}_c$. As in panel (a), the plasma contribution further enhances the shadow size.

In the combined limit $\tilde{v}_2 = 0$ and $\omega_c = 0$, the standard Schwarzschild value $R_{\rm sh} = 3\sqrt{3}M$ is recovered.

B. Inhomogeneous plasma

We next consider an inhomogeneous plasma with power-law profile $\omega_p^2(r) = z_0/r^q$ and analyze two representative cases, $q = 1$ and $q = 3$.

For both values of q, the qualitative dependence of the shadow radius on the matter parameters remains unchanged: $R_{\rm sh}$ decreases with increasing $\tilde{v}_2$ and increases with increasing $\tilde{v}_c$.

Quantitative differences emerge, however, between the two plasma profiles. For $q = 1$, increasing the plasma strength parameter z_0 produces a noticeable outward shift of the shadow. The slowly decaying plasma density therefore retains a significant refractive influence near the photon sphere.

In contrast, for $q = 3$, the plasma effect is strongly suppressed. The curves corresponding to different z_0 values nearly coincide, indicating that the shadow is primarily governed by the geometry. The rapid radial decay of the plasma density reduces its contribution at radii relevant for the photon sphere.

For $\tilde{v}_c = 0$ and $\omega_p(r) = 0$, the spacetime reduces to the Reissner–Nordström–type configuration governed by $\tilde{v}_2$, and the shadow approaches the corresponding vacuum value.

C. Shadow-based consistency analysis and Bayesian inference for Sgr A*

We now examine the consistency of the deformation parameters $(\tilde{v}_2, \tilde{v}_c)$ with the shadow-size measurement of Sgr A* reported by the Event Horizon Telescope (EHT) [53]. Following Ref. [26], we adopt the model-independ-

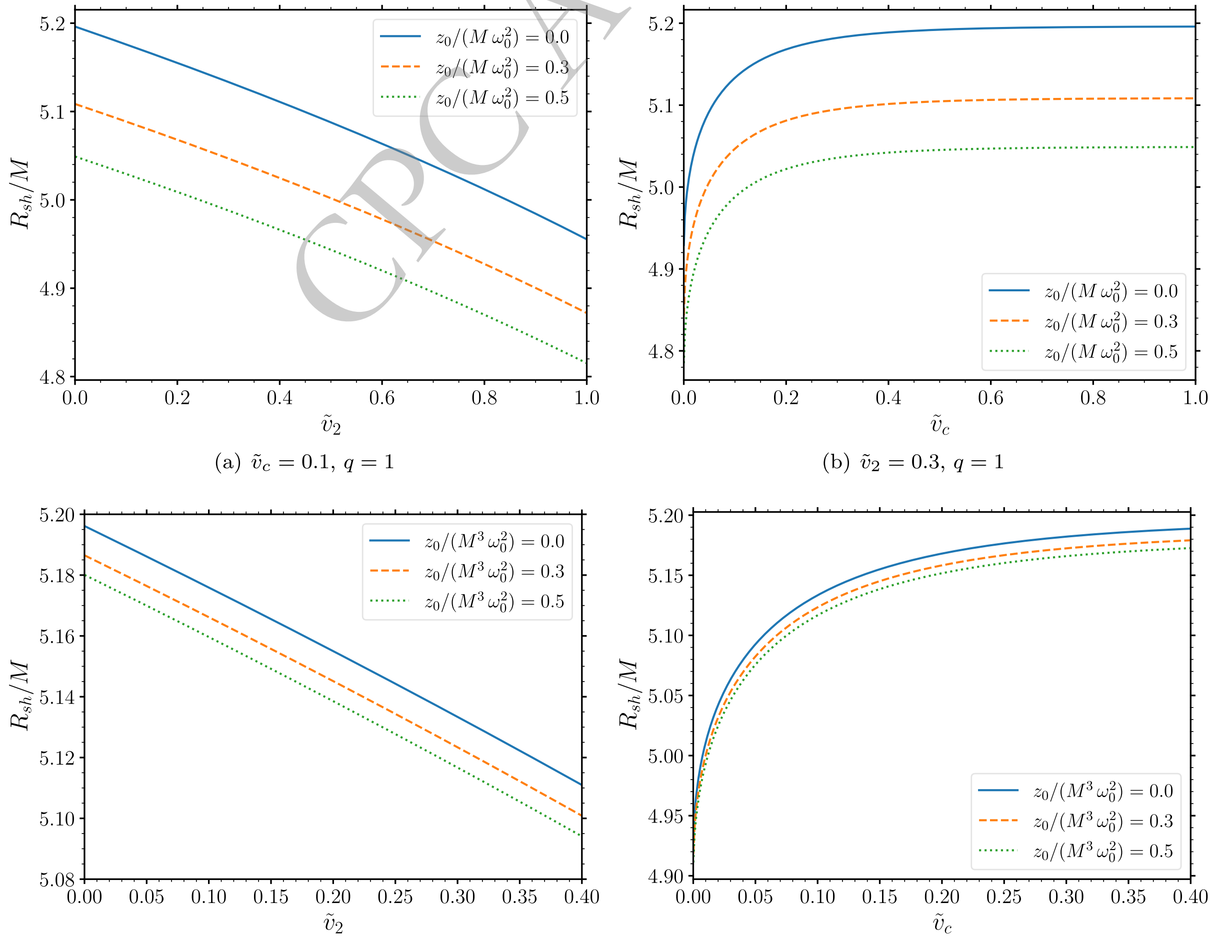

(a) $\tilde{v}_c = 0.1$, $q = 1$ (b) $\tilde{v}_2 = 0.3$, $q = 1$

(c) $\tilde{v}_c = 0.1$, $q = 3$ (d) $\tilde{v}_2 = 0.3$, $q = 3$

Fig. 6. (color online) Shadow radius $R_{\rm sh}/M$ for an inhomogeneous plasma with power-law profile $\omega_p^2(r) = z_0/r^q$. Top row: $q = 1$; bottom row: $q = 3$.

ent observational ranges for the dimensionless shadow radius

$$1\sigma: \qquad 4.55 \lesssim R_{\rm sh}/M \lesssim 5.22, \tag{25}$$

$$2\sigma: \qquad 4.21 \lesssim R_{\rm sh}/M \lesssim 5.56. \tag{26}$$

As a first consistency test, Fig. 7 shows the parameter-space regions compatible with these observational intervals using a direct interval-overlap criterion. The solid and dashed white curves represent the 1σ and 2σ boundaries, respectively, corresponding to constant values of $R_{\rm sh}/M$ within the observationally allowed range. The black solid line denotes the horizon boundary separating

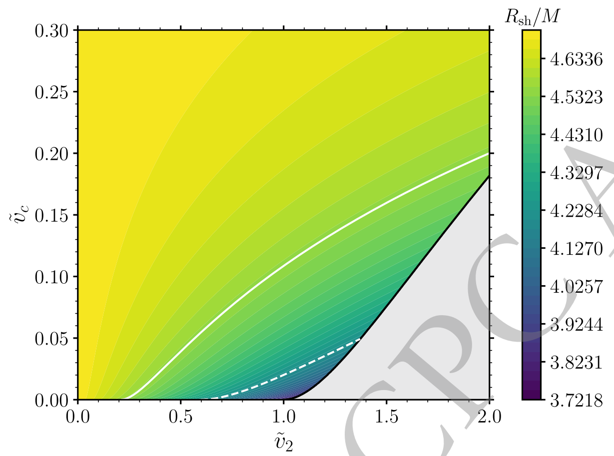

(a) Homogeneous plasma with $\omega_p^2/\omega_0^2 = 0.5$

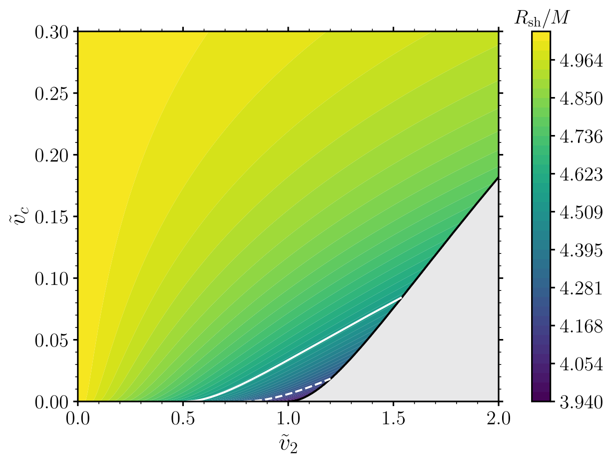

(b) Inhomogeneous plasma with $\omega_p^2/\omega_0^2 = 0.5/r$

Fig. 7. (color online) Constraints on $(\tilde{v}_2, \tilde{v}_c)$ from the shadow radius $R_{\rm sh}/M$ of the Sgr A*. The solid and dashed white contour lines correspond to the EHT 1σ and 2σ observational bounds, respectively, corresponding to $R_{\rm sh}/M \in [4.55, 5.22]$ and $R_{\rm sh}/M \in [4.21, 5.56]$. The gray region corresponds to horizonless configurations (NoBH).

black hole configurations from horizonless solutions, while the gray region corresponds to the NoBH sector.

Within the physically admissible black hole region, the shadow radius exhibits a nontrivial dependence on the deformation parameters. Increasing $\tilde{v}_2$ generally reduces the shadow size by strengthening the matter-induced deformation near the photon sphere, whereas increasing $\tilde{v}_c$ tends to enlarge the shadow by exponentially localizing the matter distribution and weakening its influence at larger radii. This competition produces curved consistency bands in the $(\tilde{v}_2, \tilde{v}_c)$ plane.

To improve upon this interval-based approach and incorporate a statistical interpretation, we additionally perform a Bayesian inference analysis [54] using a Gaussian likelihood centered on the EHT-inspired shadow radius and imposing a uniform prior over the black hole sector of the parameter space. The resulting posterior distributions are shown in Fig. 8 for both homogeneous and inhomogeneous plasma models.

For the homogeneous plasma model, the posterior median values are found to be

$$\tilde{v}_2 = 0.79^{+0.70}_{-0.55}, \qquad \tilde{v}_c = 0.19^{+0.08}_{-0.10}, \tag{27}$$

while for the inhomogeneous plasma profile $\omega_p^2 = 0.5/r$, we obtain

$$\tilde{v}_2 = 0.86^{+0.66}_{-0.58}, \qquad \tilde{v}_c = 0.18^{+0.08}_{-0.10}. \tag{28}$$

The Bayesian posterior distributions reveal a clear degeneracy between $\tilde{v}_2$ and $\tilde{v}_c$, indicating that the shadow observable primarily constrains correlated parameter combinations rather than the individual parameters independently. Physically, this degeneracy originates from the competing roles of the matter amplitude and its decay scale: stronger matter deformation (larger $\tilde{v}_2$) can be partially compensated by faster exponential suppression (larger $\tilde{v}_c$), yielding similar photon sphere configurations and therefore similar shadow sizes.

Comparing the homogeneous and inhomogeneous plasma cases, we find that the posterior structure remains qualitatively stable, with only minor shifts in the preferred parameter values. This indicates that the observed parameter degeneracy is primarily a geometric feature of the matter-deformed spacetime rather than a plasma-model artifact.

V. STRONG GRAVITATIONAL LENSING IN PLASMA

A. Deflection angle formalism

We now investigate the strong gravitational lensing of

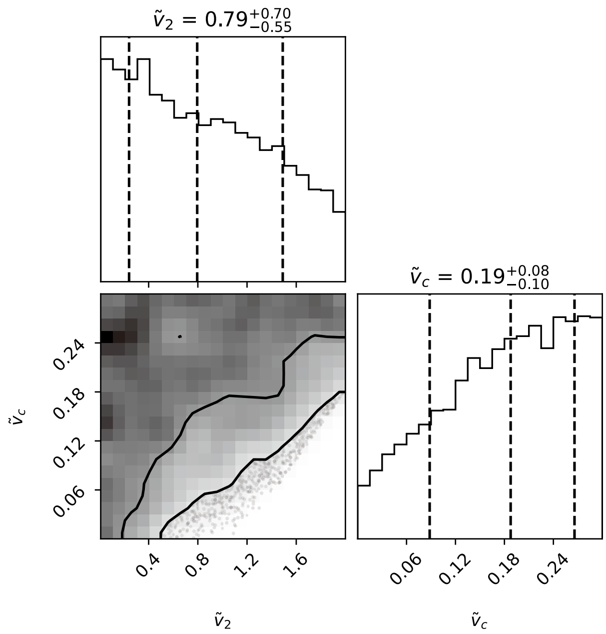

(a) Homogeneous plasma with $\omega_p^2/\omega_0^2 = 0.5$

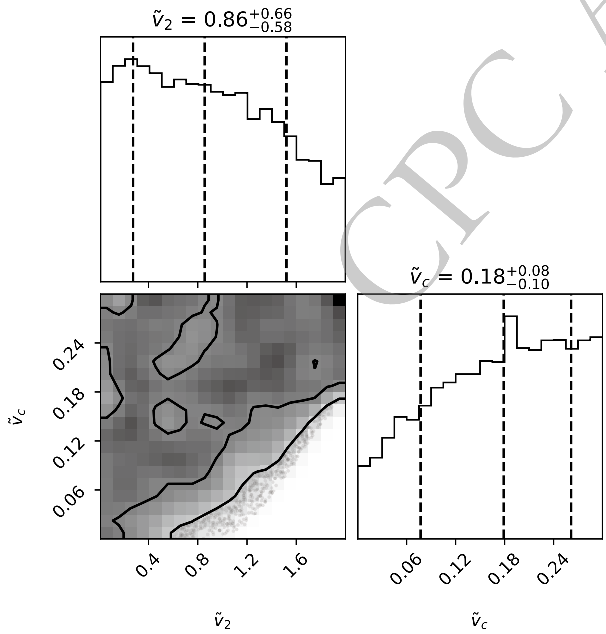

(b) Inhomogeneous plasma with $\omega_p^2/\omega_0^2 = 0.5/r$

Fig. 8. Bayesian posterior distributions of the deformation parameters $(\tilde{\nu}_2, \tilde{\nu}_c)$ inferred from the EHT-inspired shadow radius of Sgr A*. The contours represent the 68 % and 95 % credible regions.

light propagating through a cold, non-magnetized plasma surrounding the black hole described by the metric (7). Photon motion is governed by the Hamiltonian constraint $H = 0$, which yields [55]

$$-\frac{p_t^2}{f(r)} + f(r)p_r^2 + \frac{p_\phi^2}{r^2} + \omega_p^2(r) = 0, \tag{29}$$

where $p_t = -\omega_0$ is the conserved photon energy at infinity.

Using Eqs. (17-18) and eliminating p_r from Eq. (29), the phase trajectory becomes

$$\frac{d\phi}{dr} = \frac{p_\phi}{r^2 f(r) p_r} = \pm\frac{b}{r^2}\frac{1}{\sqrt{\frac{1}{f(r)} - \frac{b^2}{r^2} - \frac{\omega_p^2(r)}{\omega_0^2}}}, \tag{30}$$

where $b = p_\phi/\omega_0$ is the impact parameter.

At the turning point $r = R$, where $dr/d\phi = 0$, the impact parameter satisfies

$$b = h(R) = R\sqrt{\frac{1}{f(R)} - \frac{\omega_p^2(R)}{\omega_0^2}}, \tag{31}$$

establishing the direct relation between b and the closest approach distance.

The total azimuthal change is then [56]

$$\Delta\phi(b) = 2\int_{R(b)}^{\infty} \frac{dr}{r\sqrt{f(r)}} \frac{1}{\sqrt{h^2(r)/b^2 - 1}}, \tag{32}$$

and the deflection angle is

$$\hat{\alpha}(b) = \Delta\phi(b) - \pi. \tag{33}$$

As $b \to b_{\rm cr} = h(r_{\rm ph})$, the deflection angle diverges logarithmically, a characteristic feature of strong-field lensing associated with the unstable photon orbit.

B. Numerical implementation

The integral in Eq. (32) contains an integrable square-root divergence at $r = R$. To improve numerical stability, we introduce the transformation $x = 1 - R/r$, which yields [57]

$$\Delta\phi = 2\int_0^1 \frac{dx}{\sqrt{1-x}} \frac{1}{\sqrt{\frac{h^2(R/(1-x))}{h^2(R)} - 1}} \frac{1}{\sqrt{f(R/(1-x))}}. \tag{34}$$

This form is well suited for adaptive quadrature methods. For a given b, Eq. (31) is first solved numerically to obtain R, and the integral is then evaluated.

C. Results and analysis

Fig. 9 shows the deflection angle as a function of the impact parameter for fixed spacetime parameters $\tilde{\nu}_2 = 0.3$ and $\tilde{\nu}_c = 0.1$. In all cases, $\hat{\alpha}$ diverges as $b \to b_{\rm cr}^+$, confirming the presence of the unstable photon sphere and the ex-

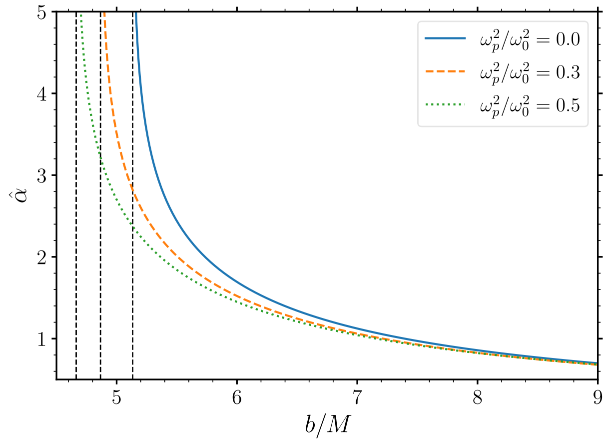

(a) Homogeneous plasma

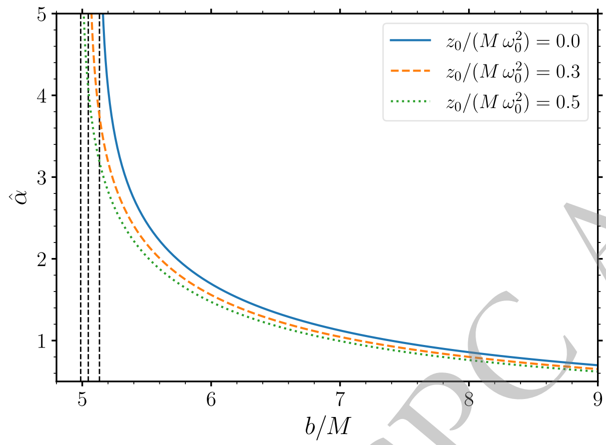

(b) Inhomogeneous plasma $\omega_p^2 = z_0/r$

Fig. 9. (color online) Deflection angle $\hat{\alpha}$ as a function of impact parameter b/M for $\tilde{v}_2 = 0.3$, $\tilde{v}_c = 0.1$. Vertical dashed lines indicate the critical impact parameter $b_{\rm cr}$.

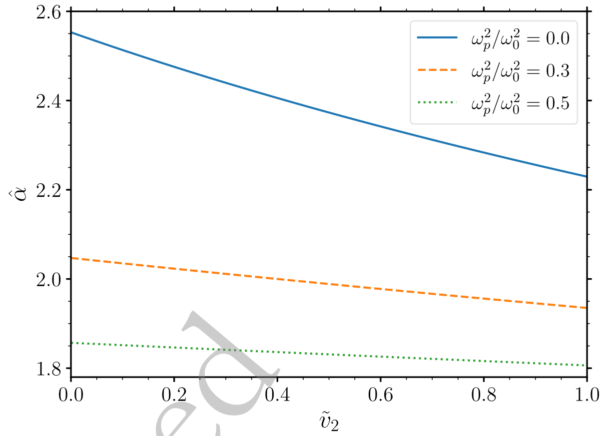

(a) $\tilde{v}_c = 0.1$

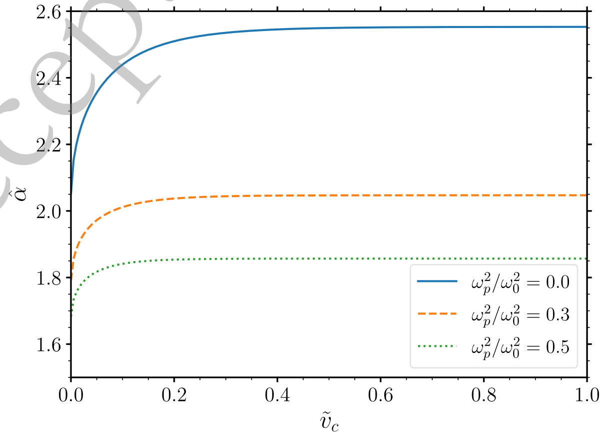

(b) $\tilde{v}_2 = 0.3$

Fig. 10. (color online) Dseflection angle $\hat{\alpha}$ versus the deformation parameters for fixed impact parameter $b = 5.5M$.

pected logarithmic strong-deflection behavior.

For fixed impact parameter b, fixed spacetime parameters $(\tilde{v}_2, \tilde{v}_c)$, and fixed photon frequency ω_0, increasing the plasma frequency systematically reduces the deflection angle. This behavior originates from the dispersive term $-\omega_p^2/\omega_0^2$ entering the effective impact function $h^2(r)$, which modifies the optical geometry and reduces the effective bending experienced by the photon trajectory. As a result, the vacuum configuration produces the largest deflection angle. The homogeneous plasma induces a stronger suppression than the inhomogeneous profile $\omega_p^2 = z_0/r$, since its refractive contribution remains significant over a broader radial range.

Fig. 10 illustrates the dependence of the deflection angle on the deformation parameters. In Fig. 10(a), with $\tilde{v}_c$ fixed, the Schwarzschild limit ($\tilde{v}_2 = 0$) yields the maximum deflection. Increasing $\tilde{v}_2$ decreases $\hat{\alpha}$ monotonically, indicating that this parameter weakens the effective gravitational focusing of light. In Fig. 10(b), with $\tilde{v}_2$ fixed, the case $\tilde{v}_c = 0$ corresponds to the RN-like limit. Increasing $\tilde{v}_c$ enhances the deflection angle, reflecting a strengthening of the near-horizon curvature and an outward shift of the photon sphere. The rapid rise at small $\tilde{v}_c$ followed by saturation suggests that the spacetime approaches a stabilized configuration in which further increases of $\tilde{v}_c$ produce only minor changes in the photon region.

In all cases, for fixed impact parameter and fixed spacetime parameters, plasma effects reduce the bending angle while preserving the qualitative dependence on the deformation parameters.

VI. CONCLUSIONS

In this work, we have investigated the optical properties of a static, spherically symmetric black hole spacetime sourced by an effective anisotropic matter distribution in the presence of a cold, non-magnetized plasma. The geometry is characterized by two deformation parameters, $\tilde{v}_2$ and $\tilde{v}_c$, which modify the Schwarzschild solution and interpolate toward a Reissner–Nordström–type configuration in appropriate limits.

We first analyzed the photon sphere structure and showed that the deformation parameters influence the unstable circular photon orbit in qualitatively distinct ways. In particular, increasing $\tilde{v}_2$ shifts the photon sphere inward, while increasing $\tilde{v}_c$ moves it outward. This opposite behavior can be understood from the competing roles of the matter amplitude and its spatial decay scale: $\tilde{v}_2$ controls the overall strength of the matter distribution, whereas $\tilde{v}_c$ governs its exponential localization.

We then studied the black hole shadow in plasma environments. The shadow radius is jointly determined by the photon sphere location and the refractive plasma contribution evaluated at that radius. Consistent with the photon sphere behavior, increasing $\tilde{v}_2$ reduces the shadow size, while increasing $\tilde{v}_c$ enlarges it. Using model-independent observational bounds on the dimensionless shadow radius derived from the EHT measurement of Sgr A* [26, 53], we first identified illustrative consistency regions in the $(\tilde{v}_2, \tilde{v}_c)$ parameter space through a direct interval-overlap criterion.

To provide a more systematic statistical interpretation, we further implemented a Bayesian inference analysis [54] based on the shadow-radius observable. The resulting posterior distributions reveal broad but nontrivial credible regions and show a clear degeneracy between the deformation parameters, indicating that the shadow observable primarily constrains correlated combinations of $\tilde{v}_2$ and $\tilde{v}_c$ rather than determining them independently. This degeneracy arises because stronger matter deformation can be partially compensated by faster exponential localization, leading to similar photon sphere configurations and nearly identical shadow radii.

Finally, we investigated strong gravitational lensing in the plasma environment. The deflection angle exhibits the expected logarithmic divergence near the critical impact parameter associated with the photon sphere. The deformation parameter $\tilde{v}_2$ weakens gravitational focusing, while $\tilde{v}_c$ enhances it. Plasma effects systematically suppress the bending angle for fixed impact parameter, reflecting the dispersive contribution to the effective optical geometry. The homogeneous plasma induces stronger modifications than rapidly decaying inhomogeneous plasma profiles.

Overall, our results demonstrate that plasma effects and matter-induced geometric deformations influence strong-field optical observables in complementary ways. While the spacetime deformation primarily governs the photon sphere structure and the global shadow geometry, plasma introduces frequency-dependent corrections that can partially mimic or compensate geometric effects. The requirement of horizon existence, together with EHT-inspired shadow measurements and Bayesian consistency analysis, significantly narrows the physically viable parameter region.

These findings highlight the importance of simultaneously accounting for environmental plasma and possible deviations from vacuum geometry when interpreting black hole shadow and lensing observations.

References

[1] H. C. Kim and W. Lee, The European Physical Journal C (2025), https://doi.org/10.1140/epjc/s10052-025-15008-w.
[2] R. Ruffini and J. A. Wheeler, Phys. Today **24**, 30 (1971)
[3] J. D. Bekenstein, Lett. Nuovo Cim. **4**, 737 (1972)
[4] J. D. Bekenstein, Phys. Rev. D **51**, R6608 (1995)
[5] K. e. a. E. H. T. C. Akiyama, Astrophys. J. **875**, L1 (2019), arXiv: 1906.11238[astro-ph.GA]
[6] K. e. a. E. H. T. C. Akiyama, Astrophys. J. **875**, L4 (2019), arXiv: 1906.11241[astro-ph.GA]
[7] K. e. a. E. H. T. C. Akiyama, Astrophys. J. **930**, L12 (2022), arXiv: 2311.08680[astro-ph.GA]
[8] C. M. Will, Living Rev. Rel. **17**, 4 (2014), arXiv: 1403.7377[gr-qc]
[9] R. A. Hulse and J. H. Taylor, Astrophys. J. **195**, L51 (1975)
[10] D. Psaltis, Living Rev. Rel. **11**, 9 (2008), arXiv: 0806.1531[astro-ph]
[11] N. Yunes and X. Siemens, Living Rev. Rel. **16**, 9 (2013), arXiv: 1304.3473[gr-qc]
[12] E. Berti *et al.*, Class. Quant. Grav. **32**, 243001 (2015), arXiv: 1501.07274[gr-qc]
[13] S. Chandrasekhar, The Mathematical Theory of Black Holes, Oxford University Press, New York, 1998.
[14] V. Bozza, Gen. Rel. Grav. **42**, 2269 (2010), arXiv: 0911.2187[gr-qc]
[15] K. S. Virbhadra and G. F. R. Ellis, Phys. Rev. D. **62**, 084003 (2000)
[16] P. V. P. Cunha and C. A. R. Herdeiro, Gen. Rel. Grav. **50**, 42 (2018), arXiv: 1801.00860[gr-qc]
[17] S. U. Islam, R. Kumara, and S. G. Ghosha, J. Cosmol. A. P **2020**, 030 (2020)
[18] V. Perlick, Living Rev. Rel. **7**, 9 (2004)
[19] A. Abdujabbarov, B. Ahmedov, N. Dadhich, and F. Atamurotov, Phys. Rev. D **96**, 084017 (2017)
[20] J. L. Synge, Mon. Not. R. Astron. Soc. **131**, 463 (1966)
[21] H. Falcke, F. Melia, and E. Agol, Astrophys. J. Lett. **528**, L13 (2000), arXiv: astro-ph/9912263
[22] K. Hioki and K.-I. Maeda, Phys. Rev. D **80**, 024042 (2009)
[23] F. Atamurotov, A. Abdujabbarov, and B. Ahmedov, Phys. Rev. D **88**, 064004 (2013)
[24] A. Abdujabbarov, F. Atamurotov, Y. Kucukakca, B. Ahmedov, and U. Camci, Astrophys. Space. Sci. **344**, 429 (2013), arXiv: 1212.4949[physics.gen-ph]
[25] V. Perlick and O. Y. Tsupko, Phys. Rept. **947**, 1 (2022), arXiv: 2105.07101[gr-qc]
[26] S. Vagnozzi, R. Roy, Y.-D. Tsai, L. Visinelli, M. Afrin, A. Allahyari, P. Bambhaniya, D. Dey, S. G. Ghosh, P. S. Joshi, K. Jusufi, M. Khodadi, R. K. Walia, A. Övgün, and C. Bambi, Classical and Quantum Gravity **40**, 165007 (2023)
[27] G. Mustafa, F. Atamurotov, I. Hussain, S. Shaymatov, and A. Övgün, Chin. Phys. C **46**, 125107 (2022), arXiv:

2207.07608[gr-qc]
[28] C. Bambi, Mod. Phys. Lett. A **28**, 1340018 (2013), arXiv: 1309.2895[gr-qc]
[29] T. Johannsen, Phys. Rev. D **87**, 124017 (2013), arXiv: 1304.0118[gr-qc]
[30] V. Cardoso and P. Pani, Living Rev. Rel. **22**, 4 (2019), arXiv: 1904.05363[gr-qc]
[31] V. Perlick, O. Y. Tsupko, and G. S. Bisnovatyi-Kogan, Phys. Rev. D **92**, 104031 (2015), arXiv: 1507.04217[grqc]
[32] V. Perlick and O. Y. Tsupko, Phys. Rev. D **95**, 104003 (2017), arXiv: 1702.08768[gr-qc]
[33] A. Rogers, Mon. Not. R. Astron. Soc. **451**, 17 (2015)
[34] F. Atamurotov, B. Ahmedov, and A. Abdujabbarov, Phys. Rev. D **92**, 084005 (2015), arXiv: 1507.08131[grqc]
[35] F. Atamurotov, K. Jusufi, M. Jamil, A. Abdujabbarov, and M. Azreg-Aïnou, Phys. Rev. D **104**, 064053 (2021), arXiv: 2109.08150[gr-qc]
[36] F. Atamurotov, M. Jamil, and K. Jusufi, Chin. Phys. C **47**, 035106 (2023), arXiv: 2212.12949[gr-qc]
[37] F. Sarikulov, F. Atamurotov, A. Abdujabbarov, and B. Ahmedov, European Physical Journal C **82** (2022), 10.1140/epjc/s10052-022-10711-4, cited by: 39; All Open Access, Gold Open Access.
[38] G. Z. Babar, A. Z. Babar, and F. Atamurotov, Eur. Phys. J. C. **80**, 761 (2020)
[39] G. Zaman Babar, F. Atamurotov, S. Ul Islam, and S. G. Ghosh, Phys. Rev. D **103**, 084057 (2021), arXiv: 2104.00714[gr-qc]
[40] R. Ali, X. Tiecheng, R. Babar, and A. Övgün, Int. J. Theor. Phys. **64**, 75 (2025), arXiv: 2402.07657[gr-qc]
[41] S. Kumar, A. Uniyal, and S. Chakrabarti, Phys. Rev. D **109**, 104012 (2024), arXiv: 2308.05545[gr-qc]
[42] M. M. Gohain, K. Bhuyan, and P. Chutia, Phys. Dark Univ. **49**, 102064 (2025), arXiv: 2504.00581[hep-th]
[43] A. Davlataliev, B. Narzilloev, I. Hussain, A. Abdujabbarov, and B. Ahmedov, Phys. Dark Univ. **42**, 101340 (2023)
[44] K. Kobialko, I. Bogush, and D. Gal'tsov, Phys. Rev. D **109**, 024060 (2024), arXiv: 2312.07498[gr-qc]
[45] A. Bakhodirov, B. Shodikulov, F. Atamurotov, A. Abdujabbarov, C. Zhou, and C. Yuan, Phys. Dark Univ. **49**, 102008 (2025)
[46] Z. Turakhonov, F. Atamurotov, S. G. Ghosh, and A. Abdujabbarov, Phys. Dark Univ. **48**, 101880 (2025)
[47] D. Umarov, O. Yunusov, F. Atamurotov, A. Abdujabbarov, and S. G. Ghosh, Chin. Phys. C **49**, 055102 (2025)
[48] A. Alimova, Z. Turakhonov, F. Atamurotov, and A. Abdujabbarov, Phys. Dark Univ. **47**, 101749 (2025)
[49] G. S. Bisnovatyi-Kogan and O. Y. Tsupko, Universe **3**, 57 (2017), arXiv: 1905.06615[gr-qc]
[50] J. L. Synge, *Relativity: The General Theory* (New York, : Interscience Publishers, 1960).
[51] Y. Pahlavon, F. Atamurotov, K. Jusufi, M. Jamil, and A. Abdujabbarov, Physics of the Dark Universe **45**, 101543 (2024)
[52] Y. Huang, Y.-P. Dong, and D.-J. Liu, International Journal of Modern Physics D **27**, 1850114 (2018)
[53] Event Horizon Telescope Collaboration, Akiyama, and *et al.*, Astrophys. J. Lett. **930**, L17.
[54] W. Liu, Y. Liu, D. Wu, and Y.-X. Liu, "A universal framework for horizon-scale tests of gravity with black hole shadows, " (2025), arXiv: 2511.06017[gr-qc].
[55] V. Bozza, General Relativity and Gravitation **42**, 2269 (2010)
[56] G. S. Bisnovatyi-Kogan and O. Y. Tsupko, Universe **3** (2017), 10.3390/universe3030057.
[57] V. Bozza, Phys. Rev. D **66**, 103001 (2002)